
CURVATURE DIVERSITY-DRIVEN DEFORMATION AND DOMAIN ALIGNMENT FOR POINT CLOUD

Mengxi Wu

Department of Computer Science
University of Southern California
{mengxiwu}@usc.edu

Hao Huang & Yi Fang

Department of Computer Science
New York University
{hh1811, yfang}@nyu.edu

Mohammad Rostami

Department of Computer Science
University of Southern California
{rostami}@usc.edu

ABSTRACT

Unsupervised Domain Adaptation (UDA) is crucial for reducing the need for extensive manual data annotation when training deep networks on point cloud data. A significant challenge of UDA lies in effectively bridging the domain gap. To tackle this challenge, we propose **Curvature Diversity-Driven Nuclear-Norm Wasserstein Domain Alignment (CDND)**. Our approach first introduces a *Curvature Diversity-driven Deformation Reconstruction (CurvRec)* task, which effectively mitigates the gap between the source and target domains by enabling the model to extract salient features from semantically rich regions of a given point cloud. We then propose *Deformation-based Nuclear-norm Wasserstein Discrepancy (D-NWD)*, which applies the Nuclear-norm Wasserstein Discrepancy to both *deformed and original* data samples to align the source and target domains. Furthermore, we contribute a theoretical justification for the effectiveness of D-NWD in distribution alignment and demonstrate that it is *generic* enough to be applied to **any** deformations. To validate our method, we conduct extensive experiments on two public domain adaptation datasets for point cloud classification and segmentation tasks. Empirical experiment results show that our CDND achieves state-of-the-art performance by a noticeable margin over existing approaches.

1 INTRODUCTION

Adopting deep neural network on point cloud representation learning has led to significant success in various applications, including robotics Maturana & Scherer (2015); Duan et al. (2021), autonomous vehicles Mahjourian et al. (2018); Cui et al. (2021), and scene understanding Zheng et al. (2013); Zhu et al. (2017). Most works rely on supervised learning Su et al. (2015); Wu et al. (2015); Qi et al. (2017) and assume that training and testing data are sampled from the same distribution. However, acquiring labels for training data is both time-consuming and labor-intensive. Moreover, testing data may be from a different distribution w.r.t. training data in real-world scenarios, known as ‘*domain gap*’. Unsupervised domain adaptation (UDA) offers a solution to tackle these issues by utilizing knowledge transfer from source domains with annotated data to target domains with only unlabeled data Wilson & Cook (2020); Li et al. (2020); Rostami et al. (2023). UDA is different from zero-shot learning (ZSL) Cheraghian et al. (2020; 2022); Rostami et al. (2022) in which predictions on unseen classes are done by leveraging auxiliary information without any training examples from those classes. Although UDA is well studied for 2D planner data, e.g., images, UDA for 3D point clouds has not been explored extensively due to challenges such as irregular, unstructured, and un-ordered nature of 3D point cloud data. Such irregularities exacerbate geometric variations between the source and target domains compared to the 2D planner data and make extending existing solutions nontrivial.

To address the above challenges, we propose **Curvature Diversity-Driven Nuclear-Norm Wasserstein Domain Alignment (CDND)**. Our first contribution is a deformation reconstruction method that leverages *curvature diversity* in different regions of a point cloud for domain alignment. We evaluate curvature diversity based on the entropy that captures the saliency of each region. This metric is then used to select regions for deformation and reconstruction. Unlike previous methods such as Achituve et al. (2021), our approach strategically selects regions based on their information content. Also, distinct from Zou et al. (2021), which selects regions with high curvature and classifies them into a fixed set, we select regions with low curvature diversity and focus on deforming and reconstructing these regions rather than classifying them. Our method avoids deforming semantically rich regions and enables the feature extractor to focus on extracting features from these regions. Our second contribution is the **Deformation-based Nuclear-norm Wasserstein Discrepancy (D-NWD)**. Unlike NWD, D-NWD incorporates features from both original and deformed samples when aligning the source and target domains. While including features from deformed samples creates a diverse and robust feature space that may improve model generalization under domain shift, our primary contribution lies in the theoretical analysis of D-NWD. This analysis demonstrates that D-NWD can reduce the domain gap between the source and target domains, showcasing its effectiveness. Our analysis also illustrates that D-NWD is *generic* enough to be used for any deformation method, not just the one presented in this paper. Experiments on common benchmarks for both classification and segmentation show that our approach achieves state-of-the-art performance.

2 RELATED WORKS

Domain Adaptation on Point Clouds. Despite extensive works on UDA for 2D planner image data Ganin & Lempitsky (2015); Mansour et al. (2008); Jian & Rostami (2023), only a limited number of studies Qin et al. (2019); Achituve et al. (2021); Shen et al. (2022); Zou et al. (2021); Wu & Rostami (2024) address UDA in point clouds and non-planner data spaces as extending methods for 2D data for point clouds in non-trivial. Qin *et al.* Qin et al. (2019) introduce PointDAN that integrates both local and global domain alignment strategies. They also provide the PointDA benchmark for point cloud classification under the UDA setting. Achituve *et al.* Achituve et al. (2021) propose a domain alignment technique that involves reconstruction from deformation and incorporates PointMixup Chen et al. (2020). They also introduce the PointSegDA benchmark for point cloud segmentation under the UDA setting. Zou *et al.* Zou et al. (2021) utilize two geometry-inspired self-supervised classification tasks to learn domain-invariant feature. Shen *et al.* Shen et al. (2022) introduce a self-supervised method for learning geometry-aware implicit functions to handle domain-specific variations effectively. Our work differs from these approaches by proposing more sophisticated self-supervised learning tasks and a generic theoretical framework, leading to state-of-the-art performance.

Optimal Transport for Domain Adaptation. The Wasserstein metric, known for encoding the natural geometry of probability measures within optimal transport theory, has been extensively studied for its application in domain adaptation due to its nice properties Courty et al. (2016; 2017); Stan & Rostami (2024). Gautheron *et al.* Gautheron et al. (2019) propose Wasserstein Distance Guided Representation Learning to leverage the Wasserstein distance to enhance similarities between embedded features. Lee et al. (2019); Rostami (2021); Gabourie et al. (2019) propose to use the sliced Wasserstein discrepancy instead of L_1 distance in Maximum Classifier Discrepancy Saito et al. (2018) to achieve a more geometrically meaningful intra-class divergence. Additionally, CGDM Du et al. (2021) introduces cross-domain gradient discrepancy to further mitigate domain differences. DeepJ-DOT Damodaran et al. (2018) utilizes a coupling matrix to map source samples to the target domain. Gautheron *et al.* Gautheron et al. (2019) propose a feature selection technique that addresses the domain shifts problem. Moreover, Xu *et al.* Xu et al. (2020) develop reliable weighted optimal transport, which uses spatial prototypical information and intra-domain structure to evaluate sample-level domain discrepancies, resulting in a better pairwise optimal transport plan. Finally, Fatras *et al.* Fatras et al. (2021) present an unbalanced optimal transport method combined with a mini-batch strategy to efficiently learn from large-scale datasets. In this work, we developed our D-NWD based on another previous method, NWD Chen et al. (2022).

3 PROPOSED METHOD

We begin by defining the unsupervised domain adaptation problem and then we provide an overview of our UDA approach, called **Curvature Diversity-Driven Nuclear-Norm Wasserstein Domain Alignment** (CDND), in Section 3.1. Next, we detail our main contributions: (1) the **Curvature Diversity-based Deformation Reconstruction** method (CurvRec), as discussed in Section 3.2 and Section 3.3, and (2) the **Deformation-based Nuclear-norm Wasserstein Discrepancy** (D-NWD) in Section 3.4. Following in Section 4, we present our theoretical contribution of D-NWD.

3.1 PROBLEM FORMULATION

We consider a source domain with labeled samples and a target domain, differing from the source, with unlabeled samples. Our goal is to develop a UDA model to accurately predict labels for the target domain using both the source labeled dataset and the target unlabeled dataset. Let \mathcal{S} represent the source domain, where X_s^i denotes the i -th batch of samples and y_s^i their corresponding labels. Similarly, let \mathcal{T} represent the target domain, where X_t^i is the i -th batch of samples. The feature space induced by \mathcal{S} and \mathcal{T} is denoted by Ω_o . In addition, we introduce deformed domains \mathcal{S}^d and \mathcal{T}^d , with their feature space Ω_d . We assume Ω_o and Ω_d to be disjoint and $\Omega_o \cup \Omega_d \subseteq \mathbb{R}^n$. A point cloud from the source domain is denoted as $x_s \in \mathbb{R}^{n \times 3}$ and from the target domain is $x_t \in \mathbb{R}^{n \times 3}$, where n is the number of points. The corresponding deformed point clouds are denoted by x_s^d and x_t^d , respectively.

The pipeline of our CDND is presented in Figure 1. Our model first uses a feature extractor E to obtain shape features from both source and target point clouds. To minimize domain gaps and ensure domain-invariant features, we: (1) use a curvature diversity-driven deformation reconstruction task using a reconstruction decoder h_{SSL} and (2) employ the D-NWD to align domains through a classifier C . The aligned features are then used for downstream tasks, *i.e.*, cloud classification and segmentation. The model is trained using source-labeled and target-unlabeled data.

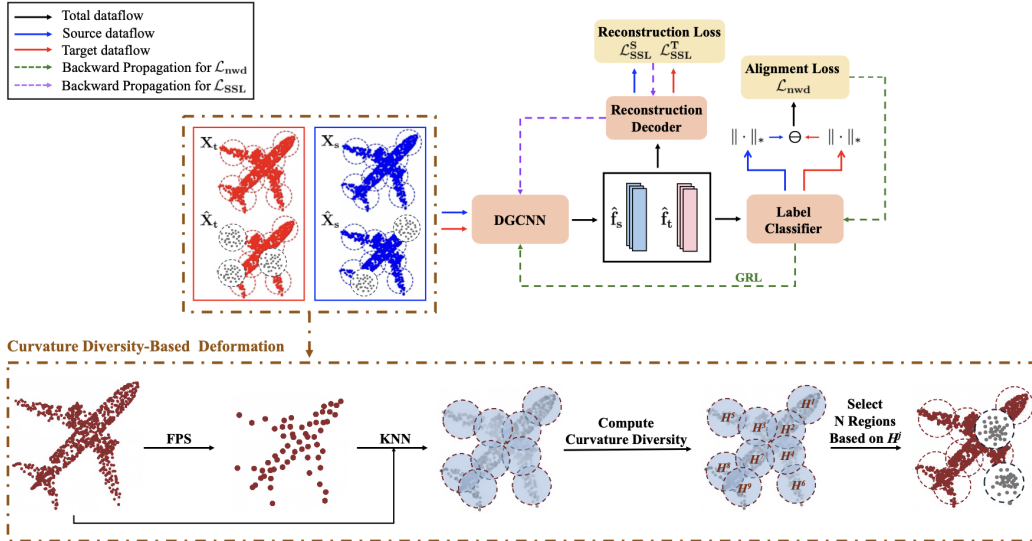


Figure 1: Pipeline of CDND. The inputs are the source batch X_s and target batch X_t . We first deform them into \hat{X}_s and \hat{X}_t using Curvature Diversity-Based Deformation. Next, X_s , X_t , \hat{X}_s , and \hat{X}_t are sent into a feature extractor. The features of deformed samples are fed into a reconstruction decoder to reconstruct the deformed regions. For domain alignment, both original and deformed features are sent to D-NWD. Aside from the two losses shown in the figure, a cross-entropy loss is computed on X_s and \hat{X}_s with labels. An NWD loss \mathcal{L}_{NWD}^T on X_t and \hat{X}_t is also computed to ensure prediction consistency between the target original and deformed pairs.

3.2 CURVATURE DIVERSITY-DRIVEN DEFORMATION

To extract domain-invariant features shared by both source and target domains, Achituve *et al.* proposed *deformation reconstruction* Achituve et al. (2021). Specifically, there are three deformation strategies introduced in Achituve et al. (2021) for deforming point clouds, *i.e.*, volume-based, feature-based, and sample-based, according to the way of dividing point clouds into regions for deformation.

Although the strategies mentioned above use different techniques to select regions for deformation, they all randomly divide a point cloud into regions and uniformly select regions based on their spatial locations or arrangements. However, this approach may not be optimal as regions within a point cloud vary in their semantic richness, *i.e.*, some regions contain more semantic information. These semantically rich regions are crucial for tasks such as classification, as they have more distinguishable characteristics. For instance, to differentiate a point cloud of a plant from that of a lamp, focusing on the leaves and flowers — which have richer semantic information — would be more effective than focusing on the flower pot, which is similar to the base of a lamp. Thus, deforming regions with richer semantic information causes the point cloud to lose semantic meaning, making it difficult for a classifier to classify it. To encourage the feature extractor to prioritize regions with rich information, we propose deforming regions that are *less* semantically rich. This strategy helps to learn to extract features from the most informative or salient regions of a point cloud.

To evaluate the richness of semantics, we propose using curvature diversity as a measurement. Following Zou *et al.* Zou et al. (2021), we compute point cloud curvature using PCA Abdi & Williams (2010). Specifically, we first select a small neighborhood around each point and apply PCA to determine the principal directions and their eigenvalues. The curvature is then calculated as:

$$c = \frac{|\lambda_{\min}|}{\sum_{i=1}^K |\lambda_i|} \quad (1)$$

where λ_{\min} is the smallest eigenvalue of the matrix, and K is the number of eigenvalues. Larger variation in curvature indicates a more intricate geometry and more significant shape changes within a region. The fourth lamp sample in the bottom row of Figure 1 illustrates this property: regions with warmer colors represent areas of higher curvature diversity. To measure the diversity or variation of curvature in a region, we propose to use *entropy of curvature*. Entropy effectively captures the variability and complexity of the curvature, allowing us to quantify the richness of semantics within a region. Formally, we use the following measure the curvature diversity:

$$\begin{aligned} c_{\min}^j &= \min_{c_i^j \in R^j} \{c_i^j\}_{i=1}^{N_{R^j}}, & c_{\max}^j &= \max_{c_i^j \in R^j} \{c_i^j\}_{i=1}^{N_{R^j}} \\ c_{i,\text{norm}}^j &= \frac{c_i^j - c_{\min}^j}{c_{\max}^j - c_{\min}^j + 1 \times 10^{-10}}, & H(c_{\text{norm}}^j) &= - \sum_{i=1}^{N_{R^j}} c_{i,\text{norm}}^j \cdot \log(c_{i,\text{norm}}^j + 1 \times 10^{-10}) \end{aligned} \quad (2)$$

where, c_i^j represents the curvatures of the i -th point in the j -th region of the point cloud which contains N_{R^j} points in total. To standardize these values, we first calculate c_{\min}^j and c_{\max}^j , which are the minimum and maximum values of all curvatures within a region, respectively. Using these values, we then normalize the curvature values to be in $[0, 1]$, denoted as $\{c_{i,\text{norm}}^j\}$. Then, we calculate the curvature diversity $H(c_{\text{norm}}^j)$ by applying entropy.¹

For the curvature diversity-driven deformation, we adopt the following steps. First, we use Farthest Point Sampling (FPS) Moenning & Dodgson (2003) to sample k points as centers of k regions. Then, for each center point, we use k -Nearest Neighbor (k -NN) to select m nearest points, *i.e.*, each region is formed by a center point along with these m nearest points. Next, we select the N regions with the *smallest* curvature diversity to deform. To deform these selected regions, we replace all the points within these regions with new points. These new points are generated by sampling from a Gaussian distribution, where the mean is set to the average position of all the original points in that region, and the variance is set to 0.001. In Figure 1, \hat{X}_s and \hat{X}_t represent the deformed samples, and the points shown in grayscale are those drawn from the Gaussian distribution.

¹Rigorously speaking, $\{c_{i,\text{norm}}^j\}$ is an un-normalized distribution without being divided by a partition function or normalization constant, but it does not affect our claim of curvature diversity.

3.3 DEFORMATION RECONSTRUCTION LOSS

After deforming the selected regions, we obtain a deformed point cloud x^d from the original x . The deformed input x^d is processed by the feature extractor E to generate $E(x^d)$, which is then passed to a reconstruction decoder h_{SSL} to reconstruct x . The self-supervised loss \mathcal{L}_{SSL} minimizes the distance between $h_{\text{SSL}}(E(x^d))$ and x . We use the Chamfer distance in \mathcal{L}_{SSL} , focusing on the original points in x within the deformed region R and their reconstructions from x^d . Formally, let $I \subset \{1, 2, \dots, m\}$ represent the indices of the points in $x \cap R$, and we define \mathcal{L}_{SSL} as:

$$\mathcal{L}_{\text{SSL}} = \sum_{(x^d, x) \in \mathcal{S} \cup \mathcal{T}} D\left(\{x_i\}_{i \in I}, \{h_{\text{SSL}}(E(x^d))_i\}_{i \in I}\right), \quad (3)$$

where x_i is the i -th point in the point cloud x and the Chamfer distance D is defined as :

$$D(R_1, R_2) = \sum_{a \in R_1} \min_{b \in R_2} \|a - b\|_2^2 + \sum_{b \in R_2} \min_{a \in R_1} \|b - a\|_2^2, \quad (4)$$

where $D(R_1, R_2)$ measures the discrepancy between point cloud regions $R_1, R_2 \subset \mathbb{R}^3$. Note that we reconstruct only the deformed regions to reduce computational resources and time.

3.4 DOMAIN ALIGNMENT VIA D-NWD

The curvature diversity-driven deformation reconstruction helps reduce the domain gap between the source and target domains. To further complete classification or segmentation tasks in the presence of domain gap, we propose D-NWD align domains, as inspired by the Nuclear-norm Wasserstein discrepancy (NWD) Chen et al. (2022). A brief overview of NWD is provided in Appendix A. Our D-NWD objective is defined as:

$$W_N(\nu_{s \cup s^d}, \nu_{t \cup t^d}) = \sup_{\|C\|_* \|L\| \leq K} \mathbb{E}_{\hat{f}_s \sim \nu_{s \cup s^d}} [\|C(\hat{f}_s)\|_*] - \mathbb{E}_{\hat{f}_t \sim \nu_{t \cup t^d}} [\|C(\hat{f}_t)\|_*] \quad (5)$$

where K is the Lipschitz constant. Here, $\nu_{s \cup s^d}$ and $\nu_{t \cup t^d}$ are probability measures defined over $\Omega_o \cup \Omega_d$, for the features from samples in original and deformed source and target domains. We align the probability measure of features from original and deformed samples in the source domain with that of the target domain. Our motivation is that taking features from deformed samples into account would provide a richer, more robust feature space, reduce overfitting, and increase the model's adaptability to variations inherent in real-world data. This differs from NWD, which aligns ν_s and ν_t defined over Ω_o , the probability measures for the features from samples in original source and target domains. Empirically, our objective in Eq. 5 be approximated by $\mathcal{L}_{\text{D-NWD}}$:

$$\mathcal{L}_{\text{D-NWD}} = \frac{1}{N_s} \sum_{i=1}^{N_s} \|C(\hat{f}_s^i)\|_* - \frac{1}{N_t} \sum_{i=1}^{N_t} \|C(\hat{f}_t^i)\|_* \quad (6)$$

where C denotes the classifier, and $\|\cdot\|_*$ represents the nuclear norm. $\hat{f}_s^i \sim \nu_{s \cup s^d}$ represents the features for the i -th source batch and $\hat{f}_t^i \sim \nu_{t \cup t^d}$ represents the features for the i -th target batch. The ratio between the original samples and deformed samples is 1:1. In practice, we obtain the original and deformed samples by first sampling from the original domain, and then generating the corresponding deformed versions. The alignment is then performed through a min-max game as:

$$\min_E \max_C \mathcal{L}_{\text{D-NWD}} \quad (7)$$

To avoid alternating updates, we employ a Gradient Reverse Layer Ganin et al. (2016), following the approach in Chen et al. (2022), to make the learned features discriminative and domain-agnostic.

3.5 OVERALL LOSS

In addition to deformation and domain alignment loss defined in Eq. 3 and Eq. 7, we use a cross-entropy loss \mathcal{L}_{CLS} on both original and deformed source domain samples for supervised training:

$$\mathcal{L}_{\text{CLS}} = \frac{1}{N_s} \sum_{i=1}^{N_s} \mathcal{L}_{\text{CE}}(C(\hat{f}_s^i), y_s^i) \quad (8)$$

Since we have no access to the ground-truth labels for the target domain data, it is impossible to use the supervised cross-entropy loss as in Eq. 8 on samples from \mathcal{T} and $\tilde{\mathcal{T}}$. One straightforward

alternative is to adopt pseudo-labels Fan et al. (2022); Liang et al. (2022); Zou et al. (2021); Shen et al. (2022). However, this strategy has the risk that the classifier might mistakenly predict target samples as the major classes of the source domain. Instead, we use NWD to ensure consistency in predictions between \mathcal{T} and \mathcal{T}^d . Thus, we define a target domain loss $\mathcal{L}_{\text{NWD}}^{\mathcal{T}}$ as:

$$\mathcal{L}_{\text{NWD}}^{\mathcal{T}} = \frac{1}{N_t} \sum_{i=1}^{N_t} \|C(f_t^i)\|_* - \frac{1}{N_t} \sum_{i=1}^{N_t} \|C(f_{t^d}^i)\|_* \quad (9)$$

where $f_{t^d}^i \sim \nu_{t^d}$ denotes the deformed target domain batch and $f_t^i \sim \nu_t$ denotes the original target domain batch. Combining Eq. 3, Eq. 8, Eq. 7 and Eq. 9 together, our overall objective loss is:

$$\begin{aligned} & \min_{E, h_{\text{SSL}}, C} \alpha \mathcal{L}_{\text{CLS}} + \gamma \mathcal{L}_{\text{SSL}} \\ & \min_E \max_C \beta_1 \mathcal{L}_{\text{D-NWD}} + \beta_2 \mathcal{L}_{\text{NWD}}^{\mathcal{T}} \end{aligned} \quad (10)$$

where $\alpha, \gamma, \beta_1, \beta_2$ are weighting hyperparameters that can be tuned using the target domain validation set. When computing the overall loss, the additional term $\mathcal{L}_{\text{NWD}}^{\mathcal{T}}$, which corresponds to $W_N(\hat{\nu}_t, \hat{\nu}_{t^d})$, does not influence our theoretical contribution of D-NWD, the bound in Eq. 14. The reason is that Eq. 14 specifically focuses on $W_N(\hat{\nu}_{s \cup s^d}, \hat{\nu}_{t \cup t^d})$, which is empirically represented by $\mathcal{L}_{\text{D-NWD}}$. The term $W_N(\hat{\nu}_t, \hat{\nu}_{t^d})$ (or $\mathcal{L}_{\text{NWD}}^{\mathcal{T}}$) is irrelevant in this context, as its influence is not directly related to the bound's conditions (or the empirical measures) being considered.

4 THEORETICAL ANALYSIS

We provide a theoretical justification for our Deformed-based Nuclear-norm Wasserstein Discrepancy (D-NWD). Following Ben-David et al. (2006) and Chen et al. (2022), we perform our analysis in a binary classification scenario, which can be easily adapted to multi-class classification through reduction techniques such as one-vs-all Rifkin & Klautau (2004) or one-vs-one Allwein et al. (2000) approaches. Consider $\{C : \mathbb{R}^n \rightarrow [0, 1]\}$ as a set of source classifiers within the hypothesis space \mathcal{H} . The risk or error of classifier C on the original source domain is defined as $\varepsilon_s(C) = \mathbb{E}_{f_s \sim \nu_s} [|C(f_s) - y_s|]$, where y_s is the label associated with the feature f_s . We then define $\varepsilon_{s \cup s^d}(C) = \mathbb{E}_{\hat{f}_s \sim \nu_{s \cup s^d}} [|C(\hat{f}_s) - \hat{y}_s|]$, where \hat{y}_s is the label associated with \hat{f}_s . Similarly, we define $\varepsilon_t(C), \varepsilon_{t \cup t^d}(C)$ as the risks on the target domain. The optimal joint hypothesis is defined as $C^* = \arg \min_C \varepsilon_{s \cup s^d}(C) + \varepsilon_t(C)$ which minimizes the combined risk across $\nu_{s \cup s^d}$ and ν_t . Our Theorem 1 demonstrates that the expected target risk $\varepsilon_t(C)$ can be bounded by the D-NWD on $\nu_{s \cup s^d}$ and $\nu_{t \cup t^d}$, $W_N(\nu_{s \cup s^d}, \nu_{t \cup t^d})$. Building on Theorem 1, we derive Theorem 2. Theorem 2 establishes that $\varepsilon_t(C)$ can be bounded by D-NWD on empirical probability measures $\hat{\nu}_{s \cup s^d}$ and $\hat{\nu}_{t \cup t^d}$, $W_N(\hat{\nu}_{s \cup s^d}, \hat{\nu}_{t \cup t^d})$. We prove Lemma 1 and 4 to support our proof of Theorem 1 and 2. **Backgrounds of 1-Wasserstein distance and NWD are in Appendix A. All proofs are included in the Appendix B.**

Lemma 1. *Let $(\Omega_1, \mathcal{F}_1, \nu_1)$ and $(\Omega_2, \mathcal{F}_2, \nu_2)$ be two probability spaces, where Ω_1, Ω_2 are two disjoint sample spaces. Let $p_1, p_2 \in [0, 1]$ be constants such that $p_1 + p_2 = 1$. Let $(\Omega_3, \mathcal{F}_3)$ be a measurable space, where \mathcal{F}_3 is the σ -algebra on $\Omega_3 = \Omega_1 \cup \Omega_2$. Then, the measure ν_3 defined on the measurable space $(\Omega_3, \mathcal{F}_3)$ as:*

$$\nu_3(A) = p_1 \nu_1(A \cap \Omega_1) + p_2 \nu_2(A \cap \Omega_2), \quad \forall A \in \mathcal{F}_3 \quad (11)$$

is a probability measure on $(\Omega_3, \mathcal{F}_3)$.

Theorem 1. *Let $(\Omega_o, \mathcal{F}_o, \nu_s)$, $(\Omega_d, \mathcal{F}_d, \nu_{s^d})$, $(\Omega_o, \mathcal{F}_o, \nu_t)$, and $(\Omega_d, \mathcal{F}_d, \nu_{t^d})$ be four probability spaces, where Ω_o and Ω_d are disjoint and $\Omega_o \cup \Omega_d \subseteq \mathbb{R}^n$. With the results of Lemma 1, let $(\Omega_o \cup \Omega_d, \mathcal{F}_u, \nu_{s \cup s^d})$ and $(\Omega_o \cup \Omega_d, \mathcal{F}_u, \nu_{t \cup t^d})$ be two probability spaces with probability measures defined as $\nu_{s \cup s^d} = 1/2 \nu_s + 1/2 \nu_{s^d}$ and $\nu_{t \cup t^d} = 1/2 \nu_t + 1/2 \nu_{t^d}$. Specifically, when sampling from $\nu_{t \cup t^d}$, there is an equal probability of 1/2 to sample from ν_t or ν_{t^d} . Similarly, sampling from $\nu_{s \cup s^d}$ gives an equal probability of 1/2 to draw from ν_s or ν_{s^d} . Let K denote a Lipschitz constant. Consider a classifier $C \in \mathcal{H}_1$ and an ideal classifier $C^* = \arg \min_C \varepsilon_{s \cup s^d}(C) + \varepsilon_t(C)$ satisfying the K -Lipschitz constraint, where \mathcal{H}_1 is a subspace of the hypothesis space \mathcal{H} . For every classifier C in \mathcal{H}_1 , the following inequality holds:*

$$\varepsilon_t(C) \leq 2\varepsilon_{s \cup s^d}(C) + 4K \cdot W_N(\nu_{s \cup s^d}, \nu_{t \cup t^d}) + \eta^* \quad (12)$$

where $\eta^* = 2\varepsilon_{s \cup s^d}(C^*) + \varepsilon_t(C^*)$ is the ideal combined risk and is a sufficiently small constant.

Definition 3 (L₁-Transportation Cost Information Inequality). Djellout et al. (2004) Given $\eta > 0$, a probability measure ν on a measurable space (Ω, \mathcal{F}) satisfies $T_1(\eta)$ if the inequality

$$W_1(\nu', \nu) \leq \sqrt{\frac{2}{\eta} H(\nu'|\nu)} \quad (13)$$

where $H(\nu'|\nu) = \int \log \frac{d\nu'}{d\nu} d\nu'$ holds for any probability measure ν' on (Ω, \mathcal{F}) , and W_1 represents the 1-Wasserstein distance.

Lemma 3. (Corollary 2.6 in Bolley & Villani (2005)) For a probability measure ν on a measurable space (Ω, \mathcal{F}) , the following statements are equivalent:

- ν satisfies $T_1(\eta)$ inequality for some η that can be explicitly found.
- ν has a square-exponential moment, i.e., there exists $\alpha > 0$ such that

$$\int_{\Omega} \exp(\alpha d(x, y)^2) d\nu(x) \text{ is finite}$$

for any $y \in \Omega$. Here, d is a measurable distance over Ω .

Lemma 4. Let $(\Omega_1, \mathcal{F}_1, \nu_1)$ and $(\Omega_2, \mathcal{F}_2, \nu_2)$ be two probability spaces, where Ω_1 and Ω_2 are disjoint. Let $p_1, p_2 \in [0, 1]$ be constants such that $p_1 + p_2 = 1$. Let $p_1, p_2 \in [0, 1]$ be constants such that $p_1 + p_2 = 1$. Define a new measure ν_3 on a measurable space $(\Omega_3, \mathcal{F}_3)$, where $\Omega_3 = \Omega_1 \cup \Omega_2$:

$$\nu_3(A) = p_1 \nu_1(A \cap \Omega_1) + p_2 \nu_2(A \cap \Omega_2), \quad \forall A \in \mathcal{F}_3$$

Suppose that ν_1 and ν_2 each has a square-exponential moment for some $\alpha_1, \alpha_2 > 0$, respectively. Then, ν_3 is a probability measure (according to Lemma 1), and ν_3 has a square-exponential moment for some $0 < \alpha < \min(\alpha_1, \alpha_2)$.

Theorem 2. (Theorem 2 of Redko et al. (2017)) Under the assumption of Theorem 1, let $(\Omega_o \cup \Omega_d, \mathcal{F}_u, \nu_{s \cup s^d})$ and $(\Omega_o \cup \Omega_d, \mathcal{F}_u, \nu_{t \cup t^d})$ be two probability spaces with $\nu_{s \cup s^d} = 1/2\nu_s + 1/2\nu_{s^d}$ and $\nu_{t \cup t^d} = 1/2\nu_t + 1/2\nu_{t^d}$, where $\nu_s, \nu_{s^d}, \nu_t, \nu_{t^d}$ each has a square-exponential moment. From Lemma 3 and 4, $\nu_{s \cup s^d}$ satisfies $T_1(\eta_s)$ for some η_s and $\nu_{t \cup t^d}$ satisfies $T_1(\eta_t)$ for some η_t . Let $F_s = \{\hat{f}_s^i\}_{i=1}^{N_s}$ and $F_t = \{\hat{f}_t^i\}_{i=1}^{N_t}$ be two sample sets of size N_s and N_t drawn i.i.d from $\nu_{s \cup s^d}$ and $\nu_{t \cup t^d}$, respectively. $\hat{\nu}_{s \cup s^d} = \frac{1}{N_s} \sum_{i=1}^{N_s} \delta_{\hat{f}_s^i}$ and $\hat{\nu}_{t \cup t^d} = \frac{1}{N_t} \sum_{i=1}^{N_t} \delta_{\hat{f}_t^i}$ are associated empirical probability measures. Then, for any $n' > n$ and $\eta' < \min(\eta_s, \eta_t)$, there exists a constant N_0 depending on n' such that for any $\delta > 0$ and $\min(N_s, N_t) \geq N_0 \max(\delta^{-(n'+2)}, 1)$, with probability at least $1 - \delta$, the following holds for all C :

$$\varepsilon_t(C) \leq 2\varepsilon_{s \cup s^d}(C) + 4K \cdot W_N(\hat{\nu}_{s \cup s^d}, \hat{\nu}_{t \cup t^d}) + \eta^* + 4K \cdot \sqrt{\frac{2}{\eta'} \log \frac{1}{\delta}} \left(\sqrt{\frac{1}{N_s}} + \sqrt{\frac{1}{N_t}} \right) \quad (14)$$

where $\eta^* = 2\varepsilon_{s \cup s^d}(C^*) + \varepsilon_t(C^*)$ is the ideal combined risk and is a sufficiently small constant.

In Equation 14, η^* are sufficiently small constants for relevant domains with consistent labels because C^* is the error corresponding the ideal classifier. The term $\sqrt{\frac{2}{\eta'} \log \frac{1}{\delta}} \left(\sqrt{\frac{1}{N_s}} + \sqrt{\frac{1}{N_t}} \right)$ is also a small constant when N_s and N_t are large. $\varepsilon_{s \cup s^d}(C)$ is minimized by a supervised classification loss, since source domain samples have labels. Therefore, the primary objective of our UDA task is to minimize our D-NWD on $\hat{\nu}_{s \cup s^d}$ and $\hat{\nu}_{t \cup t^d}$, $W_N(\hat{\nu}_{s \cup s^d}, \hat{\nu}_{t \cup t^d})$. Hence, minimizing D-NWD can improve the model's performance on samples from the original target domain \mathcal{T} . Note that we do not claim that our bound (Eq. 14) is tighter than the one in Theorem 2 Chen et al. (2022), which aligns $\hat{\nu}_s$ and $\hat{\nu}_t$, the empirical probability measures of features from samples in \mathcal{S} and \mathcal{T} . In fact, a direct comparison between the two bounds is not feasible, as they apply to different probability measures: $(\hat{\nu}_{s \cup s^d}, \hat{\nu}_{t \cup t^d})$ for D-NWD and $(\hat{\nu}_s, \hat{\nu}_t)$ for NWD. Rather than providing a tighter bound, our theoretical contribution lies in the fact that, regardless of the deformation method used, optimizing the D-NWD on $\hat{\nu}_{s \cup s^d}$ and $\hat{\nu}_{t \cup t^d}$ can effectively reduce the error on the samples from \mathcal{T} . In other words, D-NWD mitigates the negative effects of domain gaps and enhances performance on \mathcal{T} , as NWD does. However, unlike NWD, D-NWD includes features from deformed samples. This inclusion accounts for a more diverse and robust feature space, improving model generalization under domain shifts. Our empirical results show that with carefully designed deformation techniques, like our proposed CurvRec, D-NWD can outperform NWD in practice.

5 EXPERIMENTS

We evaluate our method on the **PointDA-10** Qin et al. (2019) dataset, a domain adaptation dataset for point cloud classification, and on **PointSegDA** Achituve et al. (2021), a dataset for point cloud segmentation. For the PointDA-10 dataset, we compare our approach against the recent state-of-the-art methods for point cloud domain adaptation, including **DANN** Ganin et al. (2016), **PointDAN** Qin et al. (2019), **RS** Sauder & Sievers (2019), **DefRec+PCM** Achituve et al. (2021), **GAST** Zou et al. (2021), and **ImplicitPCDA** Shen et al. (2022). Additionally, we incorporate Self-Paced Self-Training (SPST) into GAST, ImplicitPCDA, and our method, as SPST is originally included in both GAST and ImplicitPCDA. For the **PointSegDA** dataset, we compare our method with **RS**, **DefRec+PCM**, **GAST**, **ImplicitPCDA**, and **Adapt-SegMap** Tsai et al. (2018). We exclude SPST for this dataset. The reason is in Appendix C. For both datasets, we also evaluate two upper bounds: **Supervised-T**, which involves training exclusively on labeled target samples, and **Supervised**, which uses both labeled source and target samples. Additionally, we assess a lower bound, **Unsupervised**, which utilizes only labeled source samples.

5.1 DATASETS

PointDA-10 consists of three domains: ShapeNet-10 Chang et al. (2015), ModelNet-10 Wu et al. (2015), and ScanNet-10 Dai et al. (2017), each sharing ten distinct classes. **PointSegDA** consists of four domains: ADOBE, FAUST, MIT, and SCAPE. These domains share eight distinct classes of human body parts but vary in point distribution, pose, and scanned humans.

5.2 TRAINING SCHEME

Following the literature, we use DGCNN as the feature extractor Achituve et al. (2021) for fair comparison. We train the model of each method three times using distinct random seeds for initialization and report the average accuracy and standard deviation. To ensure a fair comparison, we maintain the same seed for data shuffling and use the Adam optimizer Kingma & Ba (2014) for optimization.

Models	MS	MS ⁺	SM	SS ⁺	S ⁺ M	S ⁺ S	Avg
Supervised-T	93.9 \pm 0.2	78.4 \pm 0.6	96.2 \pm 0.1	78.4 \pm 0.6	96.2 \pm 0.4	93.9 \pm 0.2	89.5
Unsupervised	83.3 \pm 0.7	43.8 \pm 2.3	75.5 \pm 1.8	42.5 \pm 1.4	63.8 \pm 3.9	64.2 \pm 0.8	62.2
DANN	75.3 \pm 0.6	41.5 \pm 0.2	62.5 \pm 1.4	46.1 \pm 2.8	53.3 \pm 1.2	63.2 \pm 1.2	57.0
PointDAN	82.5 \pm 0.8	47.7 \pm 1.0	77.0 \pm 0.3	48.5 \pm 2.1	55.6 \pm 0.6	67.2 \pm 2.7	63.1
RS	81.5 \pm 1.2	35.2 \pm 5.9	71.9 \pm 1.4	39.8 \pm 0.7	61.0 \pm 3.3	63.6 \pm 3.4	58.8
DefRec+PCM	81.7 \pm 0.6	51.8 \pm 0.3	78.6 \pm 0.7	54.5 \pm 0.3	73.7 \pm 1.6	71.1 \pm 1.4	68.6
GAST	82.3 \pm 0.6	53.0 \pm 1.1	72.6 \pm 1.9	47.6 \pm 1.5	64.6 \pm 1.5	66.8 \pm 0.6	64.5
GAST+SPST	84.5 \pm 0.5	54.1 \pm 1.8	80.1 \pm 4.6	46.7 \pm 0.6	81.5 \pm 1.7	66.7 \pm 1.1	68.9
ImplicitPCDA	79.5 \pm 0.4	41.7 \pm 1.3	72.9 \pm 1.0	47.5 \pm 2.9	67.6 \pm 5.2	66.4 \pm 0.9	62.6
ImplicitPCDA+SPST	81.3 \pm 2.2	33.2 \pm 13.4	73.2 \pm 3.4	38.0 \pm 4.6	66.9 \pm 7.7	75.0 \pm 2.7	61.3
CDND	84.1 \pm 0.3	58.7 \pm 0.8	76.2 \pm 0.0	55.7 \pm 1.0	75.1 \pm 1.5	72.0 \pm 1.9	70.3
CDND+SPST	85.4 \pm 1.1	57.6 \pm 1.3	85.0 \pm 2.2	54.5 \pm 1.1	82.6 \pm 0.7	74.6 \pm 4.4	73.3

Table 1: Performance results (accuracy) on PointDA-10 dataset.

Models	MS	MS ⁺	SM	SS ⁺	S ⁺ M	S ⁺ S	Avg
NWD	83.3 \pm 0.7	46.7 \pm 1.7	75.5 \pm 1.8	48.9 \pm 2.5	63.8 \pm 3.9	66.7 \pm 1.9	64.2
DefRec	83.4 \pm 0.5	46.9 \pm 2.3	74.5 \pm 0.9	46.3 \pm 0.6	67.7 \pm 2.3	64.0 \pm 0.8	64.0
DefRec+NWD	83.4 \pm 0.5	51.2 \pm 3.0	74.5 \pm 0.9	53.7 \pm 3.8	67.7 \pm 2.3	68.5 \pm 2.4	66.5
DefRec+D-NWD	83.4 \pm 0.5	53.1 \pm 2.3	74.5 \pm 0.9	54.6 \pm 1.0	67.7 \pm 2.3	67.4 \pm 0.1	66.8
CurvRec(S)-High	83.8 \pm 0.9	52.0 \pm 1.4	78.0 \pm 1.0	45.9 \pm 3.8	72.5 \pm 1.4	66.7 \pm 1.1	66.5
CurvRec(S)-Low	83.1 \pm 0.9	53.0 \pm 1.9	74.9 \pm 0.8	44.7 \pm 1.2	74.8 \pm 0.9	65.9 \pm 0.2	66.1
CurvRec(En)-High	82.9 \pm 1.5	52.1 \pm 0.4	77.0 \pm 0.3	46.7 \pm 1.0	70.9 \pm 0.6	65.8 \pm 0.4	65.9
CurvRec(En)-Low	84.1 \pm 0.3	52.2 \pm 1.3	76.2 \pm 0.0	50.1 \pm 0.3	75.1 \pm 1.5	66.4 \pm 1.5	67.4
CurvRec(En)-Low+PCM	83.0 \pm 0.5	53.7 \pm 1.0	74.0 \pm 0.6	54.8 \pm 1.1	73.8 \pm 1.1	76.8 \pm 0.9	69.4
CurvRec(En)-Low+NWD	84.1 \pm 0.2	54.3 \pm 2.2	76.2 \pm 0.0	52.7 \pm 2.1	75.1 \pm 1.5	70.6 \pm 2.2	68.8
CDND (CurvRec(En)-Low+D-NWD)	84.1 \pm 0.3	58.7 \pm 0.8	76.2 \pm 0.0	55.7 \pm 1.0	75.1 \pm 1.5	72.0 \pm 1.9	70.3

Table 2: Ablation study results (accuracy) on PointDA-10 dataset.

Models	FA	FM	FS	MA	MF	MS	AF	AM	AS	SA	SF	SM	AVG
Supervised	80.9 \pm 7.2	81.8 \pm 0.3	82.4 \pm 1.2	80.9 \pm 7.2	84.0 \pm 1.8	82.4 \pm 1.2	84.0 \pm 1.8	81.8 \pm 0.3	82.4 \pm 1.2	80.9 \pm 7.2	84.0 \pm 1.8	81.8 \pm 0.3	82.3
Unsupervised	78.5 \pm 0.4	60.9 \pm 0.6	66.5 \pm 0.6	26.6 \pm 3.5	33.6 \pm 1.3	69.9 \pm 1.2	38.5 \pm 2.2	31.2 \pm 1.4	30.0 \pm 3.6	74.1 \pm 1.0	68.4 \pm 2.4	64.5 \pm 0.5	53.6
AdaptSegMap	70.5 \pm 3.4	60.1 \pm 0.6	65.3 \pm 1.3	49.1 \pm 9.7	54.0 \pm 0.5	62.8 \pm 7.6	44.2 \pm 1.7	35.4 \pm 0.3	35.1 \pm 1.4	70.1 \pm 2.5	67.7 \pm 1.4	63.8 \pm 1.2	56.5
RS	78.7 \pm 0.5	60.7 \pm 0.4	66.9 \pm 0.4	59.6 \pm 5.0	38.4 \pm 2.1	70.4 \pm 1.0	44.0 \pm 0.6	30.4 \pm 0.5	36.6 \pm 0.8	70.7 \pm 0.8	73.0 \pm 1.5	65.3 \pm 1.3	57.9
DefRec+PCM	78.8 \pm 0.2	60.9 \pm 0.8	63.6 \pm 0.1	48.1 \pm 0.4	48.6 \pm 2.4	70.1 \pm 0.8	46.9 \pm 1.0	33.2 \pm 0.3	37.6 \pm 0.1	66.3 \pm 1.7	66.5 \pm 1.0	62.6 \pm 0.2	56.9
GAST	76.7 \pm 2.3	55.0 \pm 1.0	60.3 \pm 1.0	52.1 \pm 4.4	35.2 \pm 0.4	69.6 \pm 1.2	43.3 \pm 3.7	25.9 \pm 3.6	30.8 \pm 4.0	57.4 \pm 10.6	66.1 \pm 1.3	64.6 \pm 0.5	53.1
ImplicitPCDA	47.5 \pm 0.6	53.2 \pm 1.0	54.2 \pm 3.4	51.1 \pm 1.6	64.0 \pm 1.3	56.1 \pm 4.2	44.1 \pm 0.9	42.3 \pm 1.3	40.5 \pm 1.2	49.7 \pm 2.1	70.6 \pm 1.4	55.0 \pm 2.5	52.4
CDND	81.5 \pm 2.0	60.7 \pm 0.5	61.4 \pm 0.5	68.6 \pm 1.4	47.2 \pm 1.4	67.7 \pm 1.4	43.6 \pm 0.5	35.3 \pm 2.2	40.1 \pm 1.5	77.5 \pm 0.5	70.4 \pm 1.1	65.1 \pm 0.3	59.9

Table 3: Performance results (mIoU) on PointSegDA dataset.

5.3 RESULTS

Results on PointDA. The results are presented in Table 1. We use S⁺ to represent the ScanNet dataset, M to represent ModelNet, and S to represent the ShapeNet dataset. The CDND model shows significant improvement over the other approaches on the PointDA-10 dataset with the highest average accuracy of 70.3%, outperforming all other models. CDND delivers state-of-the-art performance on five out of six tasks. It excels in tasks with a large domain gap, such as MS⁺, S⁺M, SS⁺, and S⁺S. In these tasks, one domain is a synthetic dataset and another domain is a real-world dataset. This shows its proficiency in handling complex transformations. Especially, CDND scores 58.7% on MS⁺, outperforming the second-best method by approximately 6%. Additionally, CDND maintains competitive accuracy in tasks with a small domain gap, such as SM and MS, with scores of 84.1% and 76.2%, respectively. With SPST, the performance is further improved, as CDND+SPST achieves 73.3%, outperforming GAST+SPST by 4.4% and ImplicitPCDA+SPST by 12%. Note that plain CDND also outperforms both GAST+SPST and ImplicitPCDA+SPST on average. The strong performance of CDND across various tasks highlights its ability to adapt to diverse domain challenges, making it a promising choice for point cloud classification in the UDA setting.

Results on PointSegDA. The results are presented in Table 3. We use A to represent the ADOBE dataset, F to represent the FAUST dataset, M to represent the MIT dataset, and S to represent the SCAPE dataset. On the PointSegDA benchmark, CDND achieves the highest average score of 59.9, which surpasses the second-best method, RS, by a margin of 2.0%, which is significant in terms of mIoU on the segmentation task. Its superior performance is particularly evident in MA and SA tasks; in the MA task, CDND achieves a mIoU of 68.6, outperforming RS by 9%. Similarly, in the SA task, CDND secures a mIoU of 77.5, which is around 7% higher than RS. These results showcase its adaptability and learning capability. Additionally, in the FA task, CDND achieves a score of 81.5, even slightly surpassing the supervised baseline. In other tasks, *i.e.*, FM, AS, and SM tasks, CDND either matches or comes very close to the top-performing models, validating its status as a consistently high-performing model. The widespread dominance across various tasks on the PointSegDA benchmark further emphasizes CDND’s effectiveness.

5.4 ABLATION STUDY

To demonstrate the effectiveness of each component of CDND, we conduct ablative studies on the PointDA-10 dataset. There are several ways to evaluate curvature diversity. While standard deviation is commonly used to evaluate the diversity of data points, we propose using entropy. We compare our entropy-based approach (CurvRec(En)) with a standard deviation-based method (CurvRec(S)). To validate our hypothesis that focusing on low curvature diversity regions can improve performance, we investigate the impact of deforming areas with both high (CurvRec(En)+High, CurvRec(S)+High) and low (CurvRec(En)+Low, CurvRec(S)+Low) diversity.

Effectiveness of CurvRec. From Table 2, when comparing CurvRec(En) variants with CurvRec(S) variants, CurvRec(En) demonstrates better performance, with a more distinct difference between CurvRec(En)-High and CurvRec(En)-Low. This suggests that entropy is a superior method for evaluating curvature diversity in regions. In contrast, there is a much less distinction between CurvRec(S)-High and CurvRec(S)-Low. Notably, all CurvRec measures outperform DefRec, regardless of whether the focus is on high or low curvature diversity. We hypothesize that deforming regions with high curvature diversity can help the model become more robust to changes in these areas, potentially improving performance. However, all "Low" outperforms "High". This

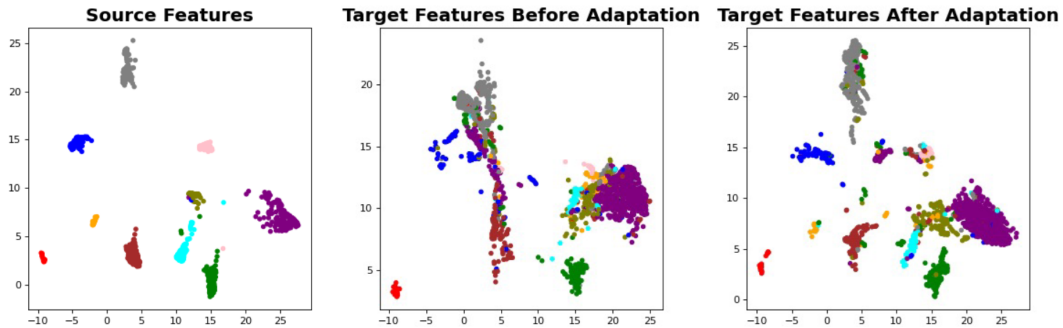


Figure 2: UMAP visualizations depict pre-activation data representations for the MS^+ task, with different colors denoting different classes. The center plot shows the target domain test data representations generated from a model trained on the source dataset without any adaptation. The left and right plots show the source and target domain data representations after adaptation using CDND.

suggests that allowing the feature extractor to concentrate on preserving and learning from the semantically rich regions is more beneficial, as altering semantically rich regions can lead to the loss of critical information. Compared to the plain NWD, all CurvRec variants perform better than plain NWD. Specifically, CurvRec(En)-Low surpasses DefRec and NWD by approximately 3%. Though CurvRec(En)-Low demonstrates better performance overall, it does not outperform our proposed CDND. CDND (CurvRec(En)-Low +D-NWD), outperforms all CurvRec variants, DefRec variants, and plain NWD. This highlights the effectiveness of our D-NWD loss. Compared to CurvRec(En)-Low, integrating with D-NWD improves average performance by 2.9%, with specific gains of 6.5% on MS^+ , 5.6% on SS^+ , and 5.6% on S^+S .

Effectiveness of D-NWD. To illustrate the effectiveness of our D-NWD, we compare CDND with two alternatives: CurvRec(En)-Low+PCM, which replaces D-NWD with PCM (PointMixup), and CurvRec(En)-Low+NWD. On average, CDND outperforms both methods. Specifically, compared to CurvRec(En)-Low+PCM, CDND achieves an improvement of approximately 5% on MS^+ , 1% on SS^+ , 1% on MS , and 2% on SM . When compared to CurvRec(En)-Low+NWD, CDND surpasses it by 4.4% on MS^+ , 3% on SS^+ , and 1.4% on S^+S . To further demonstrate that *our D-NWD can generalize to any deformation method*, we include the results of DefRec+D-NWD and DefRec+NWD. Compared to plain DefRec, DefRec+D-NWD shows an overall improvement of 2.8%, including around 6.2% on MS^+ , and 3.4% on S^+S , and a notable 8.3% on SS^+ . DefRec+D-NWD also outperforms DefRec+NWD on MS^+ and S^+S tasks, as well as on average, demonstrating that D-NWD has competitive performance compared to NWD across various deformation methods. Note that D-NWD and NWD effectively improve performance on tasks with large domain gaps, primarily between real and synthetic dataset pairs such as MS^+ and S^+S . For tasks like MS , SM , and S^+M , where the results are already strong with just CurvRec or DefRec, using D-NWD or NWD does not offer significant additional benefits. In fact, plain CurvRec and DefRec perform better in these cases, so we retain the performance of plain CurvRec or DefRec for MS , SM , and S^+M .

5.5 ANALYTIC EXPERIMENTS

We conduct analytical experiments to gain deeper insights into the effectiveness of our approach. Specifically, we assess how CDND impacts the *distribution* of the target domain in the classifier’s output space for the challenging ModelNet to ScanNet task (MS^+); ModelNet is a synthetic dataset, while ScanNet is a real-world dataset, making the domain shift between them particularly challenging. We used UMAP to visualize and compare data representations of validation data from the source domain, and test data from the target domain both before and after applying CDND. Figure 2 shows each point as a data representation in the classifier’s output space before softmax activation, with different colors denoting different classes. The middle plot in Figure 2 illustrates that, prior to adaptation, the classifier struggles with the target domain data, as points from different classes are heavily intermingled. However, after applying CDND, the class boundaries become more distinct, and the distribution of target domain representations aligns well with that of the source domain. This improvement is visible in the left and right plots of Figure 2, where the arrangement of points shows

a more distinct, consistent pattern across both domains. In other words, we see that the feature space becomes domain-agnostic. This visualization further demonstrates CDND’s efficacy in reducing domain shift-induced performance degradation and enhancing class distinction.

6 CONCLUSION

We introduced a novel unsupervised domain adaptation approach specifically for point cloud data, which presents unique challenges due to its intricate geometric structures. Our method, CDND, integrates curvature diversity-based deformation with Deformation-based Nuclear-norm Wasserstein discrepancy (D-NWD) to mitigate target domain performance degradation. Our theoretical analysis of D-NWD shows it minimizes an upper bound for target domain model error, thus enhancing performance. Additionally, the theoretical analysis shows that D-NWD can be applied to *any* deformation method. Experimental results indicate that our approach is highly effective, surpassing state-of-the-art methods on two major benchmarks. The success of our method in handling large domain differences highlights its adaptability and robustness. Ablation studies confirm that both core components of CDND are essential for achieving optimal performance. Future work could explore extending our approach to scenarios where both source domain data are not directly accessible due to privacy or when the two domains share a subset of their classes.

REFERENCES

- Hervé Abdi and Lynne J Williams. Principal component analysis. *Wiley interdisciplinary reviews: computational statistics*, 2(4):433–459, 2010.
- Idan Achituve, Haggai Maron, and Gal Chechik. Self-supervised learning for domain adaptation on point clouds. In *Proceedings of the IEEE/CVF winter conference on applications of computer vision*, pp. 123–133, 2021.
- Jonas Adler and Sebastian Lunz. Banach wasserstein gan. *Advances in neural information processing systems*, 31, 2018.
- Erin L Allwein, Robert E Schapire, and Yoram Singer. Reducing multiclass to binary: A unifying approach for margin classifiers. *Journal of machine learning research*, 1(Dec):113–141, 2000.
- Shai Ben-David, John Blitzer, Koby Crammer, and Fernando Pereira. Analysis of representations for domain adaptation. *Advances in neural information processing systems*, 19, 2006.
- François Bolley and Cédric Villani. Weighted csiszár-kullback-pinsker inequalities and applications to transportation inequalities. *Annales de la Faculté des sciences de Toulouse : Mathématiques*, 14(3):331–352, 2005.
- François Bolley, Arnaud Guillin, and Cédric Villani. Quantitative concentration inequalities for empirical measures on non-compact spaces. *Probability Theory and Related Fields*, 137:541–593, 2007.
- Angel X Chang, Thomas Funkhouser, Leonidas Guibas, Pat Hanrahan, Qixing Huang, Zimo Li, Silvio Savarese, Manolis Savva, Shuran Song, Hao Su, et al. Shapenet: An information-rich 3d model repository. *arXiv preprint arXiv:1512.03012*, 2015.
- Lin Chen, Huaian Chen, Zhixiang Wei, Xin Jin, Xiao Tan, Yi Jin, and Enhong Chen. Reusing the task-specific classifier as a discriminator: Discriminator-free adversarial domain adaptation. In *Proceedings of the IEEE/CVF Conference on Computer Vision and Pattern Recognition*, pp. 7181–7190, 2022.
- Yunlu Chen, Vincent Tao Hu, Efstratios Gavves, Thomas Mensink, Pascal Mettes, Pengwan Yang, and Cees GM Snoek. Pointmixup: Augmentation for point clouds. In *Computer Vision–ECCV 2020: 16th European Conference, Glasgow, UK, August 23–28, 2020, Proceedings, Part III 16*, pp. 330–345. Springer, 2020.
- Ali Cheraghian, Shafin Rahman, Dylan Campbell, and Lars Petersson. Transductive zero-shot learning for 3d point cloud classification. In *Proceedings of the IEEE/CVF winter conference on applications of computer vision*, pp. 923–933, 2020.

-
- Ali Cheraghian, Shafin Rahman, Townim F Chowdhury, Dylan Campbell, and Lars Petersson. Zero-shot learning on 3d point cloud objects and beyond. *International Journal of Computer Vision*, 130(10):2364–2384, 2022.
- Nicolas Courty, Rémi Flamary, Devis Tuia, and Alain Rakotomamonjy. Optimal transport for domain adaptation. *IEEE transactions on pattern analysis and machine intelligence*, 39(9):1853–1865, 2016.
- Nicolas Courty, Rémi Flamary, Amaury Habrard, and Alain Rakotomamonjy. Joint distribution optimal transportation for domain adaptation. *Advances in neural information processing systems*, 30, 2017.
- Yaodong Cui, Ren Chen, Wenbo Chu, Long Chen, Daxin Tian, Ying Li, and Dongpu Cao. Deep learning for image and point cloud fusion in autonomous driving: A review. *IEEE Transactions on Intelligent Transportation Systems*, 23(2):722–739, 2021.
- Angela Dai, Angel X. Chang, Manolis Savva, Maciej Halber, Thomas Funkhouser, and Matthias Nießner. Scannet: Richly-annotated 3d reconstructions of indoor scenes. In *Proc. Computer Vision and Pattern Recognition, IEEE*, 2017.
- Bharath Bhushan Damodaran, Benjamin Kellenberger, Rémi Flamary, Devis Tuia, and Nicolas Courty. Deepjdot: Deep joint distribution optimal transport for unsupervised domain adaptation. In *Proceedings of the European conference on computer vision (ECCV)*, pp. 447–463, 2018.
- H. Djellout, A. Guillin, and L. Wu. Transportation cost-information inequalities and applications to random dynamical systems and diffusions. *The Annals of Probability*, 32(3B):2702 – 2732, 2004. doi: 10.1214/009117904000000531.
- Zhekai Du, Jingjing Li, Hongzu Su, Lei Zhu, and Ke Lu. Cross-domain gradient discrepancy minimization for unsupervised domain adaptation. In *Proceedings of the IEEE/CVF conference on computer vision and pattern recognition*, pp. 3937–3946, 2021.
- Haonan Duan, Peng Wang, Yayu Huang, Guangyun Xu, Wei Wei, and Xiaofei Shen. Robotics dexterous grasping: The methods based on point cloud and deep learning. *Frontiers in Neurorobotics*, 15:658280, 2021.
- Rick Durrett. *Probability: theory and examples*, volume 49. Cambridge university press, 2019.
- Hehe Fan, Xiaojun Chang, Wanyue Zhang, Yi Cheng, Ying Sun, and Mohan Kankanhalli. Self-supervised global-local structure modeling for point cloud domain adaptation with reliable voted pseudo labels. In *Proceedings of the IEEE/CVF Conference on Computer Vision and Pattern Recognition*, pp. 6377–6386, 2022.
- Kilian Fatras, Thibault Séjourné, Rémi Flamary, and Nicolas Courty. Unbalanced minibatch optimal transport; applications to domain adaptation. In *International Conference on Machine Learning*, pp. 3186–3197. PMLR, 2021.
- Alexander J Gabourie, Mohammad Rostami, Philip E Pope, Soheil Kolouri, and Kuyngnam Kim. Learning a domain-invariant embedding for unsupervised domain adaptation using class-conditioned distribution alignment. In *2019 57th Annual Allerton Conference on Communication, Control, and Computing (Allerton)*, pp. 352–359. IEEE, 2019.
- Yaroslav Ganin and Victor Lempitsky. Unsupervised domain adaptation by backpropagation. In Francis Bach and David Blei (eds.), *Proceedings of the 32nd International Conference on Machine Learning*, volume 37 of *Proceedings of Machine Learning Research*, pp. 1180–1189, Lille, France, 07–09 Jul 2015. PMLR.
- Yaroslav Ganin, Evgeniya Ustinova, Hana Ajakan, Pascal Germain, Hugo Larochelle, François Laviolette, Mario Marchand, and Victor Lempitsky. Domain-adversarial training of neural networks. *The journal of machine learning research*, 17(1):2096–2030, 2016.

-
- Léo Gautheron, Ievgen Redko, and Carole Lartizien. Feature selection for unsupervised domain adaptation using optimal transport. In *Machine Learning and Knowledge Discovery in Databases: European Conference, ECML PKDD 2018, Dublin, Ireland, September 10–14, 2018, Proceedings, Part II 18*, pp. 759–776. Springer, 2019.
- Dayuan Jian and Mohammad Rostami. Unsupervised domain adaptation for training event-based networks using contrastive learning and uncorrelated conditioning. In *Proceedings of the IEEE/CVF International Conference on Computer Vision*, pp. 18721–18731, 2023.
- Diederik P Kingma and Jimmy Ba. Adam: A method for stochastic optimization. *arXiv preprint arXiv:1412.6980*, 2014.
- Chen-Yu Lee, Tanmay Batra, Mohammad Haris Baig, and Daniel Ulbricht. Sliced wasserstein discrepancy for unsupervised domain adaptation. In *Proceedings of the IEEE/CVF conference on computer vision and pattern recognition*, pp. 10285–10295, 2019.
- Rui Li, Qianfen Jiao, Wenming Cao, Hau-San Wong, and Si Wu. Model adaptation: Unsupervised domain adaptation without source data. In *Proceedings of the IEEE/CVF conference on computer vision and pattern recognition*, pp. 9641–9650, 2020.
- Hanxue Liang, Hehe Fan, Zhiwen Fan, Yi Wang, Tianlong Chen, Yu Cheng, and Zhangyang Wang. Point cloud domain adaptation via masked local 3d structure prediction. In *European Conference on Computer Vision*, pp. 156–172. Springer, 2022.
- Reza Mahjourian, Martin Wicke, and Anelia Angelova. Unsupervised learning of depth and ego-motion from monocular video using 3d geometric constraints. In *Proceedings of the IEEE conference on computer vision and pattern recognition*, pp. 5667–5675, 2018.
- Yishay Mansour, Mehryar Mohri, and Afshin Rostamizadeh. Domain adaptation with multiple sources. In D. Koller, D. Schuurmans, Y. Bengio, and L. Bottou (eds.), *Advances in Neural Information Processing Systems*, volume 21. Curran Associates, Inc., 2008.
- Daniel Maturana and Sebastian Scherer. Voxnet: A 3d convolutional neural network for real-time object recognition. In *2015 IEEE/RSJ international conference on intelligent robots and systems (IROS)*, pp. 922–928. IEEE, 2015.
- Carsten Moenning and Neil A Dodgson. Fast marching farthest point sampling. Technical report, University of Cambridge, Computer Laboratory, 2003.
- Charles R Qi, Hao Su, Kaichun Mo, and Leonidas J Guibas. Pointnet: Deep learning on point sets for 3d classification and segmentation. In *Proceedings of the IEEE conference on computer vision and pattern recognition*, pp. 652–660, 2017.
- Can Qin, Haoxuan You, Lichen Wang, C-C Jay Kuo, and Yun Fu. Pointdan: A multi-scale 3d domain adaption network for point cloud representation. *Advances in Neural Information Processing Systems*, 32, 2019.
- Ievgen Redko, Amaury Habrard, and Marc Sebban. Theoretical analysis of domain adaptation with optimal transport. In *Machine Learning and Knowledge Discovery in Databases: European Conference, ECML PKDD 2017, Skopje, Macedonia, September 18–22, 2017, Proceedings, Part II 10*, pp. 737–753. Springer, 2017.
- Ryan Rifkin and Aldebaro Klautau. In defense of one-vs-all classification. *The Journal of Machine Learning Research*, 5:101–141, 2004.
- Mohammad Rostami. Lifelong domain adaptation via consolidated internal distribution. *Advances in neural information processing systems*, 34:11172–11183, 2021.
- Mohammad Rostami, Soheil Kolouri, Zak Murez, Yuri Owechko, Eric Eaton, and Kuyngnam Kim. Zero-shot image classification using coupled dictionary embedding. *Machine Learning with Applications*, 8:100278, 2022.

-
- Mohammad Rostami, Digbalay Bose, Shrikanth Narayanan, and Aram Galstyan. Domain adaptation for sentiment analysis using robust internal representations. In *Findings of the Association for Computational Linguistics: EMNLP 2023*, pp. 11484–11498, 2023.
- Kuniaki Saito, Kohei Watanabe, Yoshitaka Ushiku, and Tatsuya Harada. Maximum classifier discrepancy for unsupervised domain adaptation. In *Proceedings of the IEEE conference on computer vision and pattern recognition*, pp. 3723–3732, 2018.
- Jonathan Sauder and Bjarne Sievers. Self-supervised deep learning on point clouds by reconstructing space. *Advances in Neural Information Processing Systems*, 32, 2019.
- Yuefan Shen, Yanchao Yang, Mi Yan, He Wang, Youyi Zheng, and Leonidas J Guibas. Domain adaptation on point clouds via geometry-aware implicit. In *Proceedings of the IEEE/CVF Conference on Computer Vision and Pattern Recognition*, pp. 7223–7232, 2022.
- Serban Stan and Mohammad Rostami. Secure domain adaptation with multiple sources. *Transactions on Machine Learning Research*, 2024.
- Hang Su, Subhransu Maji, Evangelos Kalogerakis, and Erik Learned-Miller. Multi-view convolutional neural networks for 3d shape recognition. In *Proceedings of the IEEE international conference on computer vision*, pp. 945–953, 2015.
- Yi-Hsuan Tsai, Wei-Chih Hung, Samuel Schulter, Kihyuk Sohn, Ming-Hsuan Yang, and Manmohan Chandraker. Learning to adapt structured output space for semantic segmentation. In *Proceedings of the IEEE conference on computer vision and pattern recognition*, pp. 7472–7481, 2018.
- Cédric Villani et al. *Optimal transport: old and new*, volume 338. Springer, 2009.
- Garrett Wilson and Diane J Cook. A survey of unsupervised deep domain adaptation. *ACM Transactions on Intelligent Systems and Technology (TIST)*, 11(5):1–46, 2020.
- Mengxi Wu and Mohammad Rostami. Graph harmony: Denoising and nuclear-norm wasserstein adaptation for enhanced domain transfer in graph-structured data. *Transactions on Machine Learning Research*, 2024.
- Zhirong Wu, Shuran Song, Aditya Khosla, Fisher Yu, Linguang Zhang, Xiaoou Tang, and Jianxiong Xiao. 3d shapenets: A deep representation for volumetric shapes. In *Proceedings of the IEEE conference on computer vision and pattern recognition*, pp. 1912–1920, 2015.
- Renjun Xu, Pelen Liu, Liyan Wang, Chao Chen, and Jindong Wang. Reliable weighted optimal transport for unsupervised domain adaptation. In *Proceedings of the IEEE/CVF conference on computer vision and pattern recognition*, pp. 4394–4403, 2020.
- Bo Zheng, Yibiao Zhao, Joey C Yu, Katsushi Ikeuchi, and Song-Chun Zhu. Beyond point clouds: Scene understanding by reasoning geometry and physics. In *Proceedings of the IEEE Conference on Computer Vision and Pattern Recognition*, pp. 3127–3134, 2013.
- Yuke Zhu, Roozbeh Mottaghi, Eric Kolve, Joseph J Lim, Abhinav Gupta, Li Fei-Fei, and Ali Farhadi. Target-driven visual navigation in indoor scenes using deep reinforcement learning. In *2017 IEEE international conference on robotics and automation (ICRA)*, pp. 3357–3364. IEEE, 2017.
- Longkun Zou, Hui Tang, Ke Chen, and Kui Jia. Geometry-aware self-training for unsupervised domain adaptation on object point clouds. In *Proceedings of the IEEE/CVF International Conference on Computer Vision*, pp. 6403–6412, 2021.

A REVIEW OF THE 1-WASSERSTEIN DISTANCE AND NWD

We begin the review of Nuclear-norm Wasserstein by introducing 1-Wasserstein distance:

Definition 1 (1-Wasserstein distance). Adler & Lunz (2018) 1-Wasserstein distance quantifies the minimal cost of transporting mass between two probability measures that are defined on the same sample space. Let μ and ν be two probability measures over Ω . Let (Ω, d) be a metric space, where $d(x, y)$ is distance between two points x and y in Ω . $W_1(\mu, \nu)$ is formally defined as:

$$W_1(\mu, \nu) = \inf_{\gamma \in \Gamma(\mu, \nu)} \int_{\Omega \times \Omega} d(x, y) d\gamma(x, y)$$

where $\Gamma(\mu, \nu)$ is the set of all couplings of μ and ν . A coupling $\gamma \in \Gamma(\mu, \nu)$ is a joint probability distribution on $\Omega \times \Omega$ with marginals μ and ν , meaning:

$$\int_A \int_{\Omega} \gamma(x, y) dy dx = \mu(A) \quad \text{and} \quad \int_A \int_{\Omega} \gamma(x, y) dx dy = \nu(A), \quad \forall A \in \mathcal{F}$$

Kantorovich-Rubinstein Duality shows that $W_1(\mu, \nu)$ can be rewritten as:

$$W_1(\mu, \nu) = \sup_{\|h\|_L \leq K} \mathbb{E}_{x \sim \mu}[h(x)] - \mathbb{E}_{x \sim \nu}[h(x)] \quad (15)$$

where $\|\cdot\|_L$ is the Lipschitz norm and K is the Lipschitz constant.

The Nuclear-norm Wasserstein Discrepancy (NWD) Chen et al. (2022) belongs to the family of 1-Wasserstein distances, with a sophisticatedly chosen h . Below, we present the form of h in NWD. Consider a prediction matrix $P \in \mathbb{R}^{b \times K}$ predicted by the classifier C , where b represents the number of samples in a batch and K represents the number of classes. The non-negative self-correlation matrix $Z \in \mathbb{R}^{K \times K}$ is computed as $Z = P^T P$. The intra-class correlation I_a is defined as the sum of the main diagonal elements of Z , and the inter-class correlation I_e is the sum of all the off-diagonal elements of Z :

$$I_a = \sum_{i=1}^K Z_{ii}, \quad I_e = \sum_{i \neq j}^K Z_{ij}$$

In the source domain, I_a is large, and I_e is relatively small because most samples are correctly classified. Conversely, in the target domain, I_a is small, and I_e is relatively large due to the lack of supervised training on the target domain. Hence, $I_a - I_e$ can represent the discrepancy between the two domains, as $I_a - I_e$ is large for the source domain but small for the target domain. Note that $I_a = \|P\|_F^2$ can be represented as the squared Frobenius norm of P , and thus $I_a - I_e = \|P\|_F^2 - b$.² We can rewrite $P_s = C(f_s)$ and $P_t = C(f_t)$, where f_s and f_t are feature representation batches from the source and target domains, respectively. From the above analysis, we find $\|C\|_F$ gives high scores to the source domain and low scores to the target domain, so $\|C\|_F$ works as a critic function. Thus, we can set h in Eq. 15 to be $\|C\|_F$ and represent the domain discrepancy as:

$$W_F(\nu_s, \nu_t) = \sup_{\|C\|_F \leq K} \mathbb{E}_{f_s \sim \nu_s}[\|C(f_s)\|_F] - \mathbb{E}_{f_t \sim \nu_t}[\|C(f_t)\|_F]$$

where ν_s is the probability measure for features of samples in \mathcal{S} and ν_t is the probability measure for features of samples in \mathcal{T} . To enhance prediction diversity, the Frobenius norm can be replaced with the nuclear norm which maximizes the rank of P while still being bounded by the Frobenius norm Chen et al. (2022). Thus, the domain discrepancy can be rewritten as:

$$W_N(\nu_s, \nu_t) = \sup_{\|C\|_* \leq K} \mathbb{E}_{f_s \sim \nu_s}[\|C(f_s)\|_*] - \mathbb{E}_{f_t \sim \nu_t}[\|C(f_t)\|_*] \quad (16)$$

The Eq. 16 is the formal definition of NWD. It can be approximate by \mathcal{L}_{NWD} :

$$\mathcal{L}_{\text{NWD}} = \frac{1}{N_s} \sum_{i=1}^{N_s} \|C(f_s^i)\|_* - \frac{1}{N_t} \sum_{i=1}^{N_t} \|C(f_t^i)\|_*$$

where $f_s^i \sim \nu_s$ represents the features for the i -th source batch and $f_t^i \sim \nu_t$ represents the features for the i -th target batch.

$$\min_E \max_C \mathcal{L}_{\text{NWD}} \quad (17)$$

Then, the distribution alignment is achieved through a min-max game presented in Eq. 17.

²We have $\sum_{j=1}^K Z_{i,j} = 1, \forall i \in \{1, \dots, b\}$ and $j \in \{1, \dots, K\}$, and thus $I_a + I_e = b$ Chen et al. (2022).

B THEORETICAL ANALYSIS: PROOFS FOR THEOREMS

In this section, we first prove Theorem 1, which serves as the foundation for Theorem 2. Our proofs are structured as follows: we begin by proving Lemma 1, which supports a key assumption in Theorem 1. Next, we present the proof of Theorem 1. After proving Theorem 1, we prove Lemma 4 and conclude with the proof of Theorem 2.

Definition 2 (Probability Space). **Durrett (2019)** A probability space is a triple $(\Omega, \mathcal{F}, \nu)$. Ω represents the sample space, the set of all possible outcomes. \mathcal{F} represents the set of events and is a σ -algebra, which is a collection of all subsets of Ω . \mathcal{F} is closed under complements and countable unions. ν represents a probability measure on the measurable space (Ω, \mathcal{F}) . It is a function $\nu : \mathcal{F} \rightarrow [0, 1]$ that assigns to each event $A \in \mathcal{F}$ a real value $\nu(A)$ (the probability of A). ν satisfies the following three axioms:

- *Non-negativity:* For every event $A \in \mathcal{F}$, $\nu(A) \geq \nu(\emptyset) = 0$
- *Normalization:* $\nu(\Omega) = 1$
- *σ -additivity (Countable Additivity):* For any countable sequence of pairwise disjoint events $A_1, A_2, A_3, \dots \in \mathcal{F}$ (where $A_i \cap A_j = \emptyset$ for $i \neq j$),

$$\nu \left(\bigcup_{i=1}^{\infty} A_i \right) = \sum_{i=1}^{\infty} \nu(A_i)$$

Lemma 1. Let $(\Omega_1, \mathcal{F}_1, \nu_1)$ and $(\Omega_2, \mathcal{F}_2, \nu_2)$ be two probability spaces, where Ω_1, Ω_2 are two disjoint sample spaces. Let $p_1, p_2 \in [0, 1]$ be constants such that $p_1 + p_2 = 1$. Let $(\Omega_3, \mathcal{F}_3)$ be a measurable space, where \mathcal{F}_3 is the σ -algebra on $\Omega_3 = \Omega_1 \cup \Omega_2$. Then, the measure ν_3 defined on the measurable space $(\Omega_3, \mathcal{F}_3)$ as:

$$\nu_3(A) = p_1 \nu_1(A \cap \Omega_1) + p_2 \nu_2(A \cap \Omega_2), \quad \forall A \in \mathcal{F}_3$$

is a probability measure on $(\Omega_3, \mathcal{F}_3)$.

Proof. Since ν_1 and ν_2 are probability measures, they satisfy $\nu_1(B) \geq 0$ for all $B \in \mathcal{F}_1$ and $\nu_2(C) \geq 0$ for all $C \in \mathcal{F}_2$. For any set $A \in \mathcal{F}_3$, we have:

$$\nu_3(A) = p_1 \nu_1(A \cap \Omega_1) + p_2 \nu_2(A \cap \Omega_2)$$

Given that $p_1, p_2 \geq 0$ and $\nu_1(A \cap \Omega_1) \geq 0$ and $\nu_2(A \cap \Omega_2) \geq 0$, it follows that $\nu_3(A) \geq 0$. Thus, ν_3 is non-negative. Then, we need to show that $\nu_3(\Omega_1 \cup \Omega_2) = 1$. Consider:

$$\nu_3(\Omega_1 \cup \Omega_2) = p_1 \nu_1((\Omega_1 \cup \Omega_2) \cap \Omega_1) + p_2 \nu_2((\Omega_1 \cup \Omega_2) \cap \Omega_2)$$

Since $(\Omega_1 \cup \Omega_2) \cap \Omega_1 = \Omega_1$ and $(\Omega_1 \cup \Omega_2) \cap \Omega_2 = \Omega_2$, and $\nu_1(\Omega_1) = 1$ and $\nu_2(\Omega_2) = 1$, we have:

$$\nu_3(\Omega_1 \cup \Omega_2) = p_1 \cdot 1 + p_2 \cdot 1 = p_1 + p_2 = 1$$

Thus, ν_3 is normalized. Let $\{A_i\}_{i=1}^{\infty}$ be a countable collection of pairwise disjoint sets in \mathcal{F}_3 . The last part is to show σ -additivity:

$$\nu_3 \left(\bigcup_{i=1}^{\infty} A_i \right) = \sum_{i=1}^{\infty} \nu_3(A_i)$$

By definition of ν_3 ,

$$\nu_3 \left(\bigcup_{i=1}^{\infty} A_i \right) = p_1 \nu_1 \left(\left(\bigcup_{i=1}^{\infty} A_i \right) \cap \Omega_1 \right) + p_2 \nu_2 \left(\left(\bigcup_{i=1}^{\infty} A_i \right) \cap \Omega_2 \right)$$

Since the A_i are pairwise disjoint, $(\bigcup_{i=1}^{\infty} A_i) \cap \Omega_1 = \bigcup_{i=1}^{\infty} (A_i \cap \Omega_1)$, and similarly for Ω_2 . Using the σ -additivity of ν_1 and ν_2 :

$$p_1 \nu_1 \left(\bigcup_{i=1}^{\infty} (A_i \cap \Omega_1) \right) = p_1 \sum_{i=1}^{\infty} \nu_1(A_i \cap \Omega_1)$$

$$p_2 \nu_2 \left(\bigcup_{i=1}^{\infty} (A_i \cap \Omega_2) \right) = p_2 \sum_{i=1}^{\infty} \nu_2(A_i \cap \Omega_2)$$

Thus,

$$\begin{aligned} \nu_3 \left(\bigcup_{i=1}^{\infty} A_i \right) &= p_1 \sum_{i=1}^{\infty} \nu_1(A_i \cap \Omega_1) + p_2 \sum_{i=1}^{\infty} \nu_2(A_i \cap \Omega_2) \\ &= \sum_{i=1}^{\infty} (p_1 \nu_1(A_i \cap \Omega_1) + p_2 \nu_2(A_i \cap \Omega_2)) \end{aligned}$$

Since $\nu_3(A_i) = p_1 \nu_1(A_i \cap \Omega_1) + p_2 \nu_2(A_i \cap \Omega_2)$, we get:

$$\nu_3 \left(\bigcup_{i=1}^{\infty} A_i \right) = \sum_{i=1}^{\infty} \nu_3(A_i)$$

Thus, ν_3 satisfies σ -additivity. Since ν_3 satisfies non-negativity, normalization, and σ -additivity, by definition, ν_3 is a valid probability measure.

Lemma 2 (Lemma 1 Chen et al. (2022)). *Let ν, ν' be two probability measures on (Ω, \mathcal{F}) . Let $d(x, y)$ be the distance between $x \sim \nu$ and $y \sim \nu'$. W_N represents the NWD, and K denotes a Lipschitz constant. Given a family of classifiers $C \in \mathcal{H}_1$ and an ideal classifier $C^* \in \mathcal{H}_1$ satisfying the K -Lipschitz constraint, where \mathcal{H}_1 is a subspace of \mathcal{H} , the following holds for every $C, C^* \in \mathcal{H}_1$.*

$$|\varepsilon(C, C^*) - \varepsilon'(C, C^*)| \leq 2K \cdot W_N(\nu_1, \nu_2)$$

where $\varepsilon(C, C^*) = \mathbb{E}_{x \sim \nu} [|C(x) - C^*(x)|]$ and $\varepsilon'(C, C^*) = \mathbb{E}_{y \sim \nu'} [|C(y) - C^*(y)|]$.

For future notations, we define the following:

$$\begin{aligned} \varepsilon_s(C_1, C_2) &= \mathbb{E}_{f_s \sim \nu_s} [|C_1(f_s) - C_2(f_s)|] \\ \varepsilon_{s \cup s^d}(C_1, C_2) &= \mathbb{E}_{\hat{f}_s \sim \nu_{s \cup s^d}} [|C_1(\hat{f}_s) - C_2(\hat{f}_s)|] \end{aligned}$$

where C_1, C_2 are two classifiers in \mathcal{H}_1 , We define $\varepsilon_t(C_1, C_2)$ and $\varepsilon_{t \cup t^d}(C_1, C_2)$ in the same manner.

Theorem 1. *Let $(\Omega_o, \mathcal{F}_o, \nu_s)$, $(\Omega_d, \mathcal{F}_d, \nu_{s^d})$, $(\Omega_o, \mathcal{F}_o, \nu_t)$, and $(\Omega_d, \mathcal{F}_d, \nu_{t^d})$ be four probability spaces, where Ω_o and Ω_d are disjoint and $\Omega_o \cup \Omega_d \subseteq \mathbb{R}^n$. With the results of Lemma 1, let $(\Omega_o \cup \Omega_d, \mathcal{F}_u, \nu_{s \cup s^d})$ and $(\Omega_o \cup \Omega_d, \mathcal{F}_u, \nu_{t \cup t^d})$ be two probability spaces with probability measures defined as $\nu_{s \cup s^d} = 1/2\nu_s + 1/2\nu_{s^d}$ and $\nu_{t \cup t^d} = 1/2\nu_t + 1/2\nu_{t^d}$. Specifically, when sampling from $\nu_{t \cup t^d}$, there is an equal probability of 1/2 to sample from ν_t or ν_{t^d} . Similarly, sampling from $\nu_{s \cup s^d}$ gives an equal probability of 1/2 to draw from ν_s or ν_{s^d} . Let K denote a Lipschitz constant. Consider a classifier $C \in \mathcal{H}_1$ and an ideal classifier $C^* = \arg \min_C \varepsilon_{s \cup s^d}(C) + \varepsilon_t(C)$ satisfying the K -Lipschitz constraint, where \mathcal{H}_1 is a subspace of the hypothesis space \mathcal{H} . For every classifier C in \mathcal{H}_1 , the following inequality holds:*

$$\varepsilon_t(C) \leq 2\varepsilon_{s \cup s^d}(C) + 4K \cdot W_N(\nu_{s \cup s^d}, \nu_{t \cup t^d}) + \eta^*$$

where $\eta^* = 2\varepsilon_{s \cup s^d}(C^*) + \varepsilon_t(C^*)$ is the ideal combined risk and is a sufficiently small constant.

Proof. Let Z be an indicator random variable that indicates whether the sample \hat{f}_t is drawn from ν_t or ν_{t^d} :

- $Z = 0$ if the sample is from ν_{t^d} .
- $Z = 1$ if the sample is from ν_t .

By the Law of Total Expectation, we have:

$$\begin{aligned} \varepsilon_{t \cup t^d}(C, C^*) &= \mathbb{E}_{\hat{f}_t \sim \nu_{t \cup t^d}} [|C(\hat{f}_t) - C^*(\hat{f}_t)|] \\ &= \mathbb{E}_{\hat{f}_t \sim \nu_{t \cup t^d}} [|C(\hat{f}_t) - C^*(\hat{f}_t)| \mid Z = 0] P(Z = 0) \\ &\quad + \mathbb{E}_{\hat{f}_t \sim \nu_{t \cup t^d}} [|C(\hat{f}_t) - C^*(\hat{f}_t)| \mid Z = 1] P(Z = 1) \end{aligned}$$

Substituting $P(Z = 0) = p_0$ and $P(Z = 1) = p_1$,

$$\begin{aligned}\varepsilon_{t \cup t^d}(C, C^*) &= p_0 \mathbb{E}_{\hat{f}_t \sim \nu_{t \cup t^d}} [|C(\hat{f}_t) - C^*(\hat{f}_t)| | Z = 0] \\ &\quad + p_1 \mathbb{E}_{\hat{f}_t \sim \nu_{t \cup t^d}} [|C(\hat{f}_t) - C^*(\hat{f}_t)| | Z = 1]\end{aligned}$$

Recognize that $\mathbb{E}_{\hat{f}_t \sim \nu_{t \cup t^d}} [|C(\hat{f}_t) - C^*(\hat{f}_t)| | Z = 1]$ is the expectation when \hat{f}_t is drawn from ν_t ,

$$\varepsilon_t(C, C^*) = \mathbb{E}_{\hat{f}_t \sim \nu_{t \cup t^d}} [|C(\hat{f}_t) - C^*(\hat{f}_t)| | Z = 1]$$

Combining these, we get:

$$\begin{aligned}\varepsilon_{t \cup t^d}(C, C^*) &= p_0 \mathbb{E}_{\hat{f}_t \sim \nu_{t \cup t^d}} [|C(\hat{f}_t) - C^*(\hat{f}_t)| | Z = 0] + p_1 \varepsilon_t(C, C^*) \\ \frac{1}{p_1} \varepsilon_{t \cup t^d}(C, C^*) &= \frac{p_0}{p_1} \mathbb{E}_{\hat{f}_t \sim \nu_{t \cup t^d}} [|C(\hat{f}_t) - C^*(\hat{f}_t)| | Z = 0] + \varepsilon_t(C, C^*)\end{aligned}$$

Since $\frac{p_0}{p_1} \mathbb{E}_{\hat{f}_t \sim \tilde{\mathcal{T}} \cup \tilde{\mathcal{T}}^d} [|C(\hat{f}_t) - C^*(\hat{f}_t)| | Z = 0] \geq 0$,

$$\frac{1}{p_1} \varepsilon_{t \cup t^d}(C, C^*) \geq \varepsilon_t(C, C^*)$$

Substituting $p_1 = 1/2$, we obtain:

$$2\varepsilon_{t \cup t^d}(C, C^*) \geq \varepsilon_t(C, C^*)$$

Based on Lemma 2, we have:

$$|\varepsilon_{s \cup s^d}(C, C^*) - \varepsilon_{t \cup t^d}(C, C^*)| \leq 2K \cdot W_N(\nu_{s \cup s^d}, \nu_{t \cup t^d})$$

By triangular inequality,

$$\begin{aligned}\varepsilon_t(C) &\leq \varepsilon_t(C^*) + \varepsilon_t(C^*, C) \\ \varepsilon_{s \cup s^d}(C, C^*) &\leq \varepsilon_{s \cup s^d}(C) + \varepsilon_{s \cup s^d}(C^*)\end{aligned}$$

Then, we can derive:

$$\begin{aligned}\varepsilon_t(C) &\leq \varepsilon_t(C^*) + \varepsilon_t(C^*, C) \\ &\leq \varepsilon_t(C^*) + 2\varepsilon_{t \cup t^d}(C^*, C) \\ &= \varepsilon_t(C^*) + 2\varepsilon_{s \cup s^d}(C, C^*) + 2\varepsilon_{t \cup t^d}(C, C^*) - 2\varepsilon_{s \cup s^d}(C, C^*) \\ &\leq \varepsilon_t(C^*) + 2\varepsilon_{s \cup s^d}(C, C^*) + 4K \cdot W_N(\nu_{s \cup s^d}, \nu_{t \cup t^d}) \\ &\leq \varepsilon_t(C^*) + 2\varepsilon_{s \cup s^d}(C) + 2\varepsilon_{s \cup s^d}(C^*) + 4K \cdot W_N(\nu_{s \cup s^d}, \nu_{t \cup t^d}) \\ &= 2\varepsilon_{s \cup s^d}(C) + 4K \cdot W_N(\nu_{s \cup s^d}, \nu_{t \cup t^d}) + \eta^*\end{aligned}$$

Definition 3 (L₁-Transportation Cost Information Inequality). Djellout et al. (2004) Given $\eta > 0$, a probability measure ν on a measurable space (Ω, \mathcal{F}) satisfies $T_1(\eta)$ if the inequality

$$W_1(\nu', \nu) \leq \sqrt{\frac{2}{\eta} H(\nu' | \nu)}$$

where

$$H(\nu' | \nu) = \int \log \frac{d\nu'}{d\nu} d\nu'$$

holds for any probability measure ν' on (Ω, \mathcal{F}) , where W_1 represents the 1-Wasserstein distance.

Lemma 3. (Corollary 2.6 in Bolley & Villani (2005)) For a probability measure ν on a measurable space (Ω, \mathcal{F}) , the following statements are equivalent:

- ν satisfies $T_1(\eta)$ inequality for some η that can be explicitly found.
- ν has a square-exponential moment, i.e., there exists $\alpha > 0$ such that

$$\int_{\Omega} \exp(\alpha d(x, y)^2) d\nu(x) \text{ is finite}$$

for any $y \in \Omega$. Here, d is a measurable distance over Ω .

Lemma 4. Let $(\Omega_1, \mathcal{F}_1, \nu_1)$ and $(\Omega_2, \mathcal{F}_2, \nu_2)$ be two probability spaces, where Ω_1 and Ω_2 are disjoint. Let $p_1, p_2 \in [0, 1]$ be constants such that $p_1 + p_2 = 1$. Define a new measure ν_3 on a measurable space $(\Omega_3, \mathcal{F}_3)$, where $\Omega_3 = \Omega_1 \cup \Omega_2$:

$$\nu_3(A) = p_1\nu_1(A \cap \Omega_1) + p_2\nu_2(A \cap \Omega_2), \quad \forall A \in \mathcal{F}_3$$

Suppose that ν_1 and ν_2 each has a square-exponential moment:

$$\begin{aligned} \int_{\Omega_1} \exp(\alpha_1 d_1(x, y_1)^2) d\nu_1(x) &< \infty, \quad \forall y_1 \in \Omega_1 \\ \int_{\Omega_2} \exp(\alpha_2 d_2(x, y_2)^2) d\nu_2(x) &< \infty, \quad \forall y_2 \in \Omega_2 \end{aligned}$$

for some $\alpha_1, \alpha_2 > 0$, where d_1 is defined over Ω_1 and d_2 is defined over Ω_2 . Then, ν_3 is a probability measure (according to Lemma 1), and ν_3 has a square-exponential moment for some $0 < \alpha < \min(\alpha_1, \alpha_2)$.

Proof. First, we define $d : \Omega_3 \times \Omega_3 \rightarrow \mathbb{R}^+$:

$$d(x, y) = \begin{cases} d_1(x, y) & \text{if } x, y \in \Omega_1 \\ d_2(x, y) & \text{if } x, y \in \Omega_2 \\ C & \text{if } x \in \Omega_1 \text{ and } y \in \Omega_2 \text{ (or vice versa)} \end{cases}$$

where C is a finite constant chosen to ensure d is a metric on Ω_3 . d can be expressed as:

$$d(x, y) = d_1(x, y)\mathbf{1}_{x, y \in \Omega_1} + d_2(x, y)\mathbf{1}_{x, y \in \Omega_2} + C\mathbf{1}_{x \in \Omega_1, y \in \Omega_2 \text{ or } x \in \Omega_2, y \in \Omega_1}$$

where $\mathbf{1}$ is the indicator function. d_1 and d_2 are measurable by assumption. The indicator functions are measurable because $\Omega_1 \times \Omega_1$, $\Omega_2 \times \Omega_2$, and $(\Omega_1 \times \Omega_2) \cup (\Omega_2 \times \Omega_1)$ are all in the product σ -algebra $\mathcal{F}_3 \otimes \mathcal{F}_3$. Therefore, d is a sum of products of measurable functions. Hence, d is measurable. Now, for any y in Ω_1 ,

$$\begin{aligned} &\int_{\Omega_3} \exp(\alpha d(x, y)^2) d\nu_3(x) \\ &= p_1 \int_{\Omega_1} \exp(\alpha d_1(x, y)^2) d\nu_1(x) + p_2 \int_{\Omega_2} \exp(\alpha d(x, y)^2) d\nu_2(x) \\ &\leq p_1 \int_{\Omega_1} \exp(\alpha_1 d_1(x, y)^2) d\nu_1(x) + p_2 \int_{\Omega_2} \exp(\alpha C^2) d\nu_2(x) \\ &= p_1 \int_{\Omega_1} \exp(\alpha_1 d_1(x, y)^2) d\nu_1(x) + p_2 \exp(\alpha C^2) < \infty \end{aligned}$$

For any y in Ω_2 ,

$$\begin{aligned} &\int_{\Omega_3} \exp(\alpha d(x, y)^2) d\nu_3(x) \\ &= p_1 \int_{\Omega_1} \exp(\alpha d(x, y)^2) d\nu_1(x) + p_2 \int_{\Omega_2} \exp(\alpha d_2(x, y)^2) d\nu_2(x) \\ &\leq p_1 \int_{\Omega_1} \exp(\alpha C^2) d\nu_1(x) + p_2 \int_{\Omega_2} \exp(\alpha_2 d_2(x, y)^2) d\nu_2(x) \\ &= p_1 \exp(\alpha C^2) + p_2 \int_{\Omega_2} \exp(\alpha_2 d_2(x, y)^2) d\nu_2(x) < \infty \end{aligned}$$

This proves that ν_3 has a square-exponential moment for some $0 < \alpha < \min(\alpha_1, \alpha_2)$.

Lemma 5. (Theorem 1.1 of Bolley et al. (2007); Theorem 1 of Redko et al. (2017)) Let ν be a probability measure on (Ω, \mathcal{F}) where $\Omega \subseteq \mathbb{R}^n$. ν satisfies a $T_1(\eta)$ inequality. Let $\hat{\nu} = \frac{1}{N} \sum_{i=1}^N \delta_{f^i}$ be its associated empirical measure defined on a sample set $\{f^i\}_{i=1}^N$ of size N drawn i.i.d from ν . Then for any $n' > n$ and $\eta' < \eta$, there exists some constant N_0 depending on n'

and some square-exponential moment of ν such that for any $\epsilon > 0$ and $N \geq N_0 \max(\epsilon^{-(n'+2)}, 1)$, the following holds:

$$\mathbb{P}[W_N(\nu, \hat{\nu}) > \epsilon] \leq \exp\left(-\frac{\eta'}{2} N \epsilon^2\right)$$

Theorem 2. (Theorem 2 of Redko et al. (2017)) Under the assumption of Theorem 1, let $(\Omega_o \cup \Omega_d, \mathcal{F}_u, \nu_{s \cup s^d})$ and $(\Omega_o \cup \Omega_d, \mathcal{F}_u, \nu_{t \cup t^d})$ be two probability spaces with $\nu_{s \cup s^d} = 1/2\nu_s + 1/2\nu_{s^d}$ and $\nu_{t \cup t^d} = 1/2\nu_t + 1/2\nu_{t^d}$, where $\nu_s, \nu_{s^d}, \nu_t, \nu_{t^d}$ each has a square-exponential moment. From Lemma 3 and 4, $\nu_{s \cup s^d}$ satisfies $T_1(\eta_s)$ for some η_s and $\nu_{t \cup t^d}$ satisfies $T_1(\eta_t)$ for some η_t . Let $F_s = \{\hat{f}_s^i\}_{i=1}^{N_s}$ and $F_t = \{\hat{f}_t^i\}_{i=1}^{N_t}$ be two sample sets of size N_s and N_t drawn i.i.d from $\nu_{s \cup s^d}$ and $\nu_{t \cup t^d}$, respectively. $\hat{\nu}_{s \cup s^d} = \frac{1}{N_s} \sum_{i=1}^{N_s} \delta_{\hat{f}_s^i}$ and $\hat{\nu}_{t \cup t^d} = \frac{1}{N_t} \sum_{i=1}^{N_t} \delta_{\hat{f}_t^i}$ are associated empirical probability measures. Then, for any $n' > n$ and $\eta' < \min(\eta_s, \eta_t)$, there exists a constant N_0 depending on n' such that for any $\delta > 0$ and $\min(N_s, N_t) \geq N_0 \max(\delta^{-(n'+2)}, 1)$, with probability at least $1 - \delta$, the following holds for all C :

$$\varepsilon_t(C) \leq 2\varepsilon_{s \cup s^d}(C) + 4K \cdot W_N(\hat{\nu}_{s \cup s^d}, \hat{\nu}_{t \cup t^d}) + \eta^* + 4K \cdot \sqrt{\frac{2}{\eta'} \log \frac{1}{\delta}} \left(\sqrt{\frac{1}{N_s}} + \sqrt{\frac{1}{N_t}} \right)$$

where $\eta^* = 2\varepsilon_{s \cup s^d}(C^*) + \varepsilon_t(C^*)$ is the ideal combined risk and is a sufficiently small constant.

Proof. Based on Theorem 1,

$$\varepsilon_t(C) \leq 2\varepsilon_{s \cup s^d}(C) + 4K \cdot W_N(\nu_{s \cup s^d}, \nu_{t \cup t^d}) + \eta^*$$

As a part of a broader class of Wasserstein distances, W_N satisfies the axioms of a distance Villani et al. (2009). Hence, W_N satisfies the triangle inequality:

$$\begin{aligned} \varepsilon_t(C) &\leq 2\varepsilon_{s \cup s^d}(C) + 4K \cdot W_N(\nu_{s \cup s^d}, \hat{\nu}_{s \cup s^d}) + 4K \cdot W_N(\hat{\nu}_{s \cup s^d}, \nu_{t \cup t^d}) + \eta^* \\ &\leq 2\varepsilon_{s \cup s^d}(C) + 4K \cdot W_N(\nu_{s \cup s^d}, \hat{\nu}_{s \cup s^d}) + 4K \cdot W_N(\hat{\nu}_{s \cup s^d}, \hat{\nu}_{t \cup t^d}) \\ &\quad + 4K \cdot W_N(\hat{\nu}_{t \cup t^d}, \nu_{t \cup t^d}) + \eta^* \end{aligned}$$

According to Theorem 1, $\Omega_o \cup \Omega_d \subseteq \mathbb{R}^n$. Thus, from Lemma 5,

$$W_N(\nu_{s \cup s^d}, \hat{\nu}_{s \cup s^d}) \leq \sqrt{\frac{2}{\eta'} \log \left(\frac{1}{\delta}\right)} \cdot \sqrt{\frac{1}{N_s}}$$

$$W_N(\nu_{t \cup t^d}, \hat{\nu}_{t \cup t^d}) \leq \sqrt{\frac{2}{\eta'} \log \left(\frac{1}{\delta}\right)} \cdot \sqrt{\frac{1}{N_t}}$$

W_N belongs to the family of 1-Wasserstein distance. By the symmetry property of distance,

$$W_N(\hat{\nu}_{t \cup t^d}, \nu_{t \cup t^d}) = W_N(\nu_{t \cup t^d}, \hat{\nu}_{t \cup t^d}) \leq \sqrt{\frac{2}{\eta'} \log \left(\frac{1}{\delta}\right)} \cdot \sqrt{\frac{1}{N_t}}$$

Substituting back, we have:

$$\varepsilon_t(C) \leq 2\varepsilon_{s \cup s^d}(C) + 4K \cdot W_N(\hat{\nu}_{s \cup s^d}, \hat{\nu}_{t \cup t^d}) + \eta^* + 4K \cdot \sqrt{\frac{2}{\eta'} \log \left(\frac{1}{\delta}\right)} \left(\sqrt{\frac{1}{N_s}} + \sqrt{\frac{1}{N_t}} \right)$$

C EXPERIMENT DETAILS

Implementaion Details. Our code is based on the open-source implementation of the DeRec+PCM. We trained our three CDND models with seeds $\{1, 2, 3\}$ on A100 GPUs. For the PointSegDA dataset, we fixed the learning rate to be 0.001 and conducted a grid search to optimize the hyperparameters α, γ, β_1 , and β_2 for each task. The specific hyperparameter values can be found in Table 4. Similarly, for the PointDA dataset, the hyperparameters are listed in Table 5. The training time for tasks in the PointDA dataset is approximately 10 hours, resulting in a high computational cost for hyperparameter tuning. Therefore, we do not tune the hyperparameters extensively. Similarly, for GAST and ImplicitPCDA, we use the hyperparameters provided in their open-source code (GAST, ImplicitPCDA) for the PointDA dataset.

However, GAST and ImplicitPCDA have not been tested on the PointSegDA dataset before. When implementing GAST, we conduct a grid search on the PointSegDA dataset, exploring values of 0.1, 0.2, 0.5, and 1.0 for both \mathcal{L}_{rot} and \mathcal{L}_{loc} . For ImplicitPCDA, we perform a grid search on the PointSegDA dataset, considering values of 0.1, 0.2, 0.5, and 1.0 for \mathcal{L}_M . Please refer to the original papers Zou et al. (2021); Shen et al. (2022) for the definitions of \mathcal{L}_{rot} , \mathcal{L}_{loc} , and \mathcal{L}_M .

Table 4: Hyperparameters for PointSegDA.

Hyperparameter	Values
Learning Rate	0.001
α	1.0
γ	[0.05, 0.1, 0.2, 0.5, 1.0]
β_1	[0.0, 0.05, 0.1, 0.2, 0.5, 1.0]
β_2	[0.0, 0.2]

Table 5: Hyperparameters for PointDA.

Hyperparameter	Values
Learning Rate	0.001, 0.0001 (S ⁺ M, MS)
α	0.5
γ	0.5
β_1	[0.0, 1.0]
β_2	0.2

Challenges of Applying SPST with mIoU. The mIoU metric is defined as:

$$\text{mIoU} = \frac{1}{M} \sum_{m=1}^M \frac{TP_m}{TP_m + FP_m + FN_m} \quad \text{where:} \quad \begin{aligned} M &= \text{number of classes} \\ TP_m &= \text{true positive for class } m \\ FP_m &= \text{false positive for class } m \\ FN_m &= \text{false negative for class } m \end{aligned}$$

SPST typically relies on ranking training samples by difficulty and gradually incorporating harder examples into training. The training samples for point cloud segmentation tasks are points in point clouds. However, mIoU is a global metric that evaluates performance across an entire point cloud, making it challenging to assign difficulty scores to individual points in a point cloud. The mechanism of SPST mismatches the per-point cloud, rather than per-point, evaluation criterion of mIoU.